Earth and Planetary Science Letters 362 (2013) 143–150

Contents lists available at SciVerse ScienceDirect

Earth and Planetary Science Letters

journal homepage: www.elsevier.com/locate/epsl

Melting of compressed iron by monitoring atomic dynamics

Jennifer M. Jackson [a,e,*], Wolfgang Sturhahn [b], Michael Lerche [b], Jiyong Zhao [b], Thomas S. Toellner [b], E. Ercan Alp [b], Stanislav V. Sinogeikin [c], Jay D. Bass [d], Caitlin A. Murphy [a,e], June K. Wicks [e]

[a] Seismological Laboratory, California Institute of Technology, Pasadena, CA 91125, United States
[b] Advanced Photon Source, Argonne National Laboratory, Argonne, IL 60439, United States
[c] HP-CAT, Carnegie Institution of Washington, Argonne, IL 60439, United States
[d] Department of Geology, University of Illinois at Urbana-Champaign, Urbana, IL 60801, United States
[e] Division of Geological & Planetary Sciences, California Institute of Technology, Pasadena, CA 91125, United States

ARTICLE INFO

Article history:
Received 25 November 2011
Received in revised form
21 November 2012
Accepted 27 November 2012
Editor: L. Stixrude

Keywords:
iron
melting
dynamics
high-pressure
Mössbauer

ABSTRACT

We present a novel method for detecting the solid–liquid phase boundary of compressed iron at high temperatures using synchrotron Mössbauer spectroscopy (SMS). Our approach is unique because the dynamics of the iron atoms are monitored. This process is described by the Lamb–Mössbauer factor, which is related to the mean-square displacement of the iron atoms. Focused synchrotron radiation with 1 meV bandwidth passes through a laser-heated ^{57}Fe sample inside a diamond-anvil cell, and the characteristic SMS time signature vanishes when melting occurs. At our highest compression measurement and considering thermal pressure, we find the melting point of iron to be $T_M = 3025 \pm 115$ K at $P = 82 \pm 5$ GPa. When compared with previously reported melting points for iron using static compression methods with different criteria for melting, our melting trend defines a steeper positive slope as a function of pressure. The obtained melting temperatures represent a significant step toward a reliable melting curve of iron at Earth's core conditions. For other terrestrial planets possessing cores with liquid portions rich in metallic iron, such as Mercury and Mars, the higher melting temperatures for compressed iron may imply warmer internal temperatures.

1. Introduction

Seismological and cosmochemical observations indicate that Earth's core consists of a solid inner region surrounded by a liquid outer core, with iron as the main constituent, e.g., (Lehmann, 1936; McDonough and Sun, 1995; Stixrude et al., 1997; McDonough, 2003). The melting temperature of iron at high-pressure provides an important reference point for the temperature distribution within Earth's core and affects a number of important geophysical quantities related to this region: heat flow across the core–mantle boundary (CMB), the temperature gradient within the thermal boundary layer above the CMB, phase relations, and expected wave speeds of candidate phases (e.g., Anderson, 1990; Lay et al., 2008; Hemley and Mao, 2001). More specifically, the melting point of iron at the boundary between the liquid outer core and solid inner core (ICB) provides an upper bound of the temperature at that interface, because studies thus far indicate that all plausible outer core liquids coexist with corresponding inner core alloy solids at or below the melting point of pure iron (e.g., Boehler, 1992; Fei et al., 1995, 1997; Alfè et al., 2002a; Stewart et al., 2007; Chen et al., 2008; Andrault et al., 2009; Asanuma et al., 2010; Terasaki et al., 2011, and references therein). The melting temperature of iron at high-pressure provides a similarly important reference point for temperature distributions within the cores of other terrestrial planets, such as Mercury and Mars, whose cores are thought to be at least partially molten (e.g., Stevenson, 2001; Fei and Bertka, 2005; Margot et al., 2007; Smith et al., 2012).

Studies of the melting curve of highly compressed iron have been performed dynamically in shock-compression experiments (Brown and McQueen, 1986; Bass et al., 1987; Yoo et al., 1993; Ahrens et al., 2002; Nguyen and Holmes, 2004), statically in diamond-anvil cell experiments, and in calculations (Alfè et al., 1999, 2002b; Laio et al., 2000; Alfè, 2009; Sola and Alfè, 2009). Melting of iron in diamond-anvil cells was achieved by resistive heating monitored by the resistance–temperature curves of the heated wire (Boehler, 1986; Mao et al., 1987), and by laser heating combined with either visual observations (Williams et al., 1987; Boehler, 1993) or with synchrotron x-ray diffraction analysis (Shen et al., 1998; Ma et al., 2004; Boehler et al., 2008). At the ICB, reported melting temperatures of iron range from 4900 to 7600 K. Recently, an internally consistent thermodynamic database was presented for iron up to 360 GPa and 7000 K (Komabayashi and Fei, 2010), based on a newly reported phase

* Corresponding author.
E-mail address: jackson@gps.caltech.edu (J.M. Jackson).

0012-821X/$ - see front matter © 2013 Published by Elsevier B.V.
http://dx.doi.org/10.1016/j.epsl.2012.11.048

boundary between the face-centered cubic (*fcc* or γ) and hexagonal close-packed (*hcp* or ϵ) structures (Komabayashi et al., 2009) and existing thermochemical measurements. However, the complete data set of melting observations does not reflect a consensus on the melting curve of iron (see Komabayashi and Fei, 2010, for a recent review).

Here we present a new approach for detecting the melting point of compressed iron using the physical principle of recoilless absorption of x-rays by nuclear resonances (Mössbauer, 1958)—the basis of both conventional Mössbauer spectroscopy and synchrotron Mössbauer spectroscopy (SMS). In these techniques, the observed signal strength is sensitively related to the thermal motion of the resonant nuclei, ^{57}Fe in our case. This phenomenon is quantitatively described by the Lamb–Mössbauer factor, *f*, which is known to vanish when melting occurs. In this study, we show that the solid–liquid phase boundary of compressed iron can readily be monitored by the disappearance of the SMS signal upon melting. The obtained melting temperatures represent a significant step toward a reliable melting curve of iron at Earth's core conditions. Furthermore, with iron being a dominant component of candidate alloys in Earth's core and a main constituent in the mineralogy of Earth's mantle, this method should provide a unique complement to existing methods for the determination of melting curves of iron-bearing phases under high-pressure conditions.

2. Methods

2.1. Melt detection using Mössbauer spectroscopy

The physical principles of synchrotron Mössbauer spectroscopy (SMS) have been studied previously in great detail (e.g., Sturhahn, 2004, and references therein). The observed time-delayed signal is caused by the coherent elastic scattering of synchrotron x-rays while traversing a sample containing ^{57}Fe or a similar resonant isotope. The emission of the SMS signal occurs into the direction of the incident x-rays, the forward direction, and is therefore independent of the spatial configuration of atoms. The strength of the SMS signal is primarily determined by the "effective thickness" of the sample traversed by the x-rays. The effective thickness, η, is a dimensionless number given as the product of the numerical density of the ^{57}Fe nuclei, ρ, the physical thickness of the sample, *d*, the nuclear resonant cross-section, $\sigma = 2.56 \times 10^{-22}$ m^2, and the dimensionless Lamb–Mössbauer factor *f*

$$\eta = f\sigma\rho d. \tag{1}$$

The relation between SMS intensity and effective thickness is complex but can be numerically calculated in every detail (Sturhahn, 2000). Here our strategy is to determine all relevant parameters that influence the SMS signal strength with the exception of the Lamb–Mössbauer factor.

Typical values for the Lamb–Mössbauer factor for solids at room-temperature range from 0.05 to 0.9 (Sturhahn and Chumakov, 1999). A value of 0.796 ± 0.002 has been reported for body-centered cubic (*bcc* or α) iron at ambient conditions (Toellner et al., 1997), and an increase with pressure is commonly observed (Murphy et al., 2011b; Mao et al., 2001; Giefers et al., 2002). With increasing temperature, *f* typically decreases (Sturhahn and Chumakov, 1999; Bergmann et al., 1994; Shen et al., 2004). However at the solid–liquid phase transition a discontinuous drop to zero has been observed for tin metal at ambient pressure (Boyle et al., 1961). Mechanisms for this abrupt change in *f* upon melting have been discussed (Singwi and Sjölander, 1960), and may be best understood by expressing the Lamb–Mössbauer factor as $f = \exp[-k^2 \langle u^2 \rangle]$, where *k* is the wave number of the resonant x-rays and $\langle u^2 \rangle$ is the mean-square displacement of the nuclear resonant atoms. In this expression, it is implicitly assumed that the time scale for the positional averaging is determined by the lifetime of the nuclear state excited in the SMS scattering process. For example, the lifetime and the energy of the first excited state for ^{57}Fe are 141 ns and 14.4 keV, respectively. If the iron atoms stray from their equilibrium positions much farther than $1/k = 0.14$ Å during the nuclear lifetime, the value of *f* becomes exponentially small. This rarely happens for solids, but in the liquid state atoms are very mobile and move 10's of Å during 100 ns. For all practical purposes, the Lamb–Mössbauer factor therefore becomes zero for liquids leading to zero effective thickness and a collapse of the SMS signal.

The disappearance of the SMS signal is strictly based on the dynamical behavior of the atoms in a time window comparable to the nuclear lifetime. The spatial arrangement of the atoms such as crystalline order is not relevant for the collapse of the SMS signal. This is in clear contrast to the common application of x-ray diffraction techniques to determine melting. In x-ray diffraction, the x-ray scattering process is non-resonant and extremely fast, i.e., of the order of 10^{-19} s, and atomic motions become irrelevant. An x-ray diffraction pattern represents a series of snapshots of atomic positions. Each snapshot clearly reflects the spatial order of the sample. In this situation, the disappearance of features such as diffraction lines and the appearance of diffuse scattering upon melting are caused by the loss of long-range order not by a change in atomic mobility.

In the method we present here, we observe the time-integrated SMS signal $I(\eta)$ which can be expressed in terms of the theoretical time spectrum appropriate for the sample $S(t,\eta)$

$$I(\eta) = A e^{-\mu d} \sum_{n=0}^{\infty} \int_{t_1+nt_B}^{t_2+nt_B} S(t',\eta)\, dt'. \tag{2}$$

Here t_1 and t_2 are the beginning and end of the time window accessible in the experiment, t_B is the time between x-ray pulses (n) given by the synchrotron operation mode (where $n=0$ refers to the most recent x-ray pulse), *A* is a scaling factor that depends on experimental conditions such as x-ray spectral flux incident on the sample, *d* is the physical thickness of the sample, and μ is the electronic absorption coefficient of the sample material. The analysis of measured data reduces to an inversion problem with respect to the effective thickness, η. An important input to the required modeling is the shape of $S(t,\eta)$ which depends on the level splitting of the resonant nuclei. For *fcc* and *hcp* phases of iron, it is well known that the nuclear levels of ^{57}Fe are unsplit. Then the time spectrum is given as

$$S(t,\eta) = \eta^2\, e^{-t/\tau} \frac{J_1^2(x)}{x^2} \quad \text{with } x = \sqrt{\eta t/\tau}, \tag{3}$$

where J_1 is the first-order Bessel function of the first kind and τ is the lifetime of the excited nuclear state (Kagan et al., 1979). The linear behavior of the Bessel function for small arguments, $J_1(x) \approx x/2$, is followed by a regime of aperiodic oscillations and eventually by the asymptotic form for large arguments, $J_1(x) \approx (\sin x - \cos x)/\sqrt{\pi x}$. In our data analysis, we numerically solve the integration in (2) with the shape of the time spectrum given by (3) for a series of reasonable effective thickness values using the CONUSS software (Sturhahn, 2000). The effect of electronic attenuation, the exponential in (2), is important if the thickness of the sample changes during the heating cycle. Otherwise, it may be assimilated into the scaling factor. In all successful melting experiments, a continuous decrease in thickness was observed over the duration of the heating cycle (~ 0.25 μm/min, with a starting sample thickness of typically 9 μm and cycle

lasting less than 2 min). After attenuation corrections were applied, the scaling factor A is obtained by matching calculation and measurement near a characteristic region of the spectrum. Alternatively, the shape of the SMS time spectrum could be measured in detail under conditions for which the Lamb–Mössbauer factor is well known. The physical thickness as well as the scaling factor could then be derived by a fit of the data to $AS(t,\eta)$ with A and η as variables. Details of this procedure for a particular melting experiment are described in Section 2.2.

2.2. Experiments

Beveled and unbeveled diamond anvils with flat culet diameters ranging from 260 μm to 450 μm were mounted into diamond-anvil cells (DACs). A 95% isotopically enriched ^{57}Fe foil with a thickness of 10 μm was cut into rectangular sections with an electric discharge machine and cleaned. Dehydrated KCl was pressed into transparent flakes and loaded together with an ^{57}Fe foil in a sandwich configuration into a rhenium gasket pre-indented to a thickness of around 50 μm. The DACs were heated in a vacuum furnace before closing. For the highest compression point, the DAC was loaded in an inert atmosphere glove box equipped with a moisture-removal system located at sector 3 of the Advanced Photon Source (Zhao et al., 2004a). The KCl served as both a pressure-transmitting medium and thermal insulation. Rubies were placed away from the sample and used as pressure markers. The pressure was determined before and after each melting run using the R_1 fluorescence line shift (Mao et al., 1986). We report the pressure at 300 K as determined from the average of all rubies in a given sample chamber, with an error reflecting the minimum and maximum pressure. Thermal pressure is discussed in Section 3.1.

The SMS laser-heating experiments were performed at sector 3-ID-B of the Advanced Photon Source (APS) at Argonne National Laboratory (Fig. 1). The x-rays were prepared with a bandwidth of 1 meV at the 14.4 keV nuclear resonance of ^{57}Fe using a multiple-crystal Bragg reflection monochromator (Toellner, 2000). The SMS signal was recorded using an avalanche photodiode detector in forward scattering geometry. Ionization chambers were placed before and after the sample to record the x-ray intensity loss. This information allowed us to determine heating-induced thickness changes of the sample and thereby, to properly include the electronic attenuation term in Eq. (2). Thickness changes were determined from the ion chamber and electronic absorption coefficients of Fe and KCl. Typically, we found that the sample thickness decreases by $\sim$0.25 μm/min, with a starting sample thickness of typically 9 μm and cycle lasting less than 2 min. Focusing of the x-rays was obtained using a Kirkpatrick–Baez (KB) mirror system with a focal spot size measured to be 8.5 × 6.1 μm^2 at the full-width half-maximum at the sample position. Newly installed clean-up slits positioned between the KB mirrors and the DAC reduced the size to 5 × 5 μm^2 and improved the shape of the x-ray focal spot to minimize the presence of a lower-temperature solid in the x-ray scattering volume. The remaining tails of the spatial x-ray distribution that may penetrate cooler regions of the sample accounted for an estimated 10% of the total x-ray intensity.

A Nd:YLF laser operating at 1053 nm in TEM$_{01}$ mode with a focus spot size of $\sim$40 μm at ambient conditions and somewhat smaller in the DAC was used for double-sided heating of the iron samples inside the DAC (Zhao et al., 2004b; Lin et al., 2004). The system spectral response was calibrated using a standard tungsten ribbon lamp with known radiance, and greybody temperatures were determined by fitting the thermal radiation spectrum between 670 nm and 830 nm to the Planck radiation function (see Shen et al., 2001 for more details). It is important to emphasize that temperatures have been measured at sector 3-ID-B for compressed iron samples heated up to 1700 K by two independent methods: spectral radiometry (Heinz and Jeanloz, 1987; Shen et al., 2001) and the temperature-dependent intensity asymmetry of the nuclear resonant inelastic x-ray scattering (NRIXS) spectra based on the detailed balance principle (Lin et al., 2004; Shen et al., 2004; Zhao et al., 2004b; Sturhahn and Jackson, 2007). The asymmetry of the NRIXS spectra, given by the Boltzmann factor, is independent of the optical components of the laser-heating system and sample properties. The results of this procedure show that the temperature measured by the detailed balance principle and values determined from thermal radiation spectra are in very good agreement, resulting in an uncertainty of ±100 K (Zhao et al., 2004b; Lin et al., 2004; Ma et al., 2004).

Each melting run consisted of, first, aligning the x-ray and laser-heating spot on the sample at an initial starting temperature ($T \approx 1500$ K), followed by a computer-controlled sequence: the laser power was ramped up incrementally and kept constant for 2 to 5 s with the shorter time duration used for higher pressures; integrated SMS signal and ion chamber intensities were accumulated and recorded; the temperature of the heating spot was obtained by analysis of its light-emission spectrum. Two or three temperature measurements were typically averaged and recorded for each laser power level. A high-temperature run sometimes ended by hole-burning and loss of delayed counts. In our procedure, a hole was quantitatively demonstrated by an abrupt change in the intensity data from the ion chambers and thus, clearly distinct from melting. We performed measurements at pre-heating pressures ranging from 12.5 to 70 GPa with a total time for each melting run of typically less than 100 s.

For a successful melting run, the evaluation proceeded in the following order: correct the measured integrated SMS signal for electronic attenuation (this step is unnecessary if the ionization chamber intensity was constant during the melting run); match the observed trend in the delayed counts vs. laser power against the

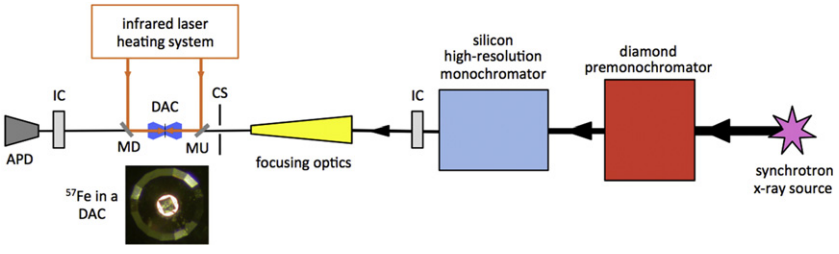

Fig. 1. Experimental set-up for SMS melting experiments at sector 3-ID-B of the APS. The 14.4 keV X-rays are monochromatized to bandwidths of an eV and 1 meV by a high-heat-load diamond premonochromator (located in 3-ID-A) and a high-resolution silicon monochromator, respectively. The sample in the water-cooled diamond-anvil cell (DAC) is positioned into the x-ray focus area. An IR laser and associated optics are located above the sample area (top-tier), with the exception of the upstream (MU) and downstream (MD) mirrors and two objective lenses (not shown) (Zhao et al., 2004b). Clean-up slits (CS) are positioned proximal to MU, and the locations of the ion chambers (IC) are shown. Delayed photons are collected by an avalanche photodiode detector (APD). The ^{57}Fe sample in the DAC is 80 × 80 μm^2.

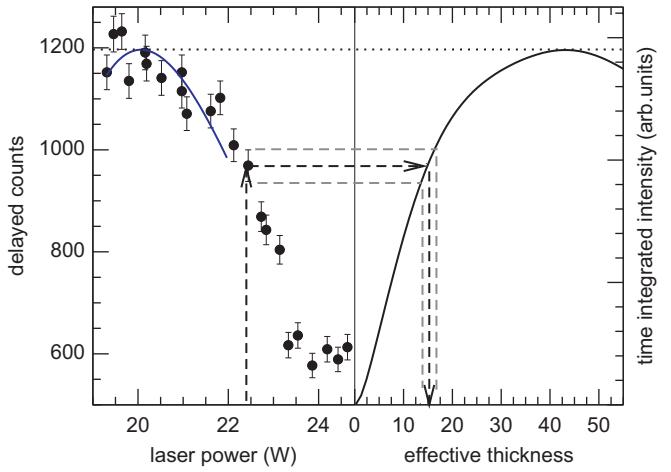

Fig. 2. Delayed counts (per 2 s) as a function of laser power at $P_{300\ K}=50\pm2$ GPa and the determination of effective thickness provided the time integrated transmission intensity. The right panel displays the calculated integrated SMS signal according to Eq. (2). The delayed counts were corrected for electronic attenuation (Eq. (2)). The blue line is a guide to the eye. Error bars are given by the square-root of measured delayed counts, and the grey dashed lines indicate how the uncertainties propagate. (For interpretation of the references to colour in this figure legend, the reader is referred to the web version of this article.)

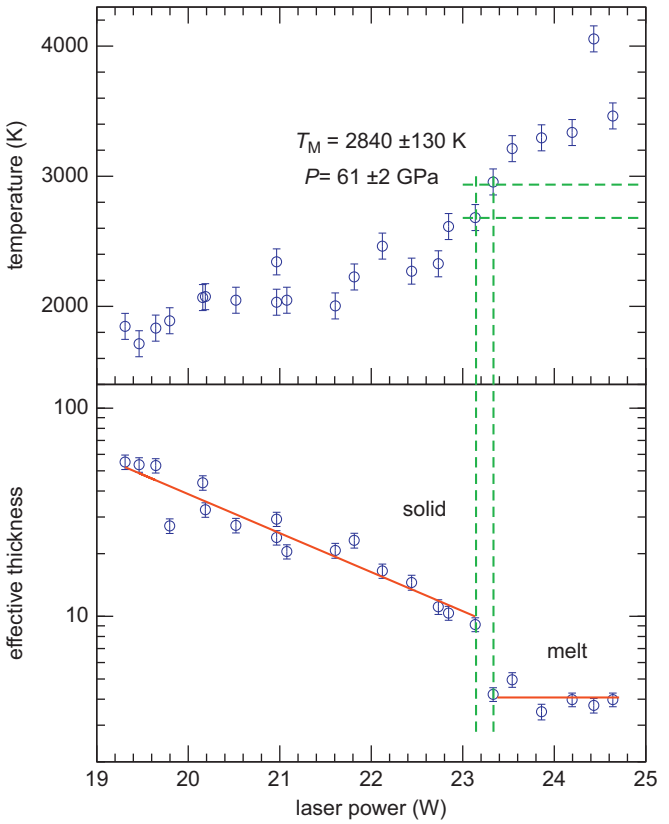

Fig. 3. Emission temperature and effective thickness as a function of laser power for the melting point determined at $P=61\pm2$ GPa ($P_{300\ K}=50\pm2$ GPa). The duration of this experimental run was ~50 s. After melting occurs, the effective thickness remains at an approximately constant non-zero value which is explained by tails of the spatial x-ray distribution penetrating cooler regions of the sample. The melting temperature is determined by the bounds of the observed solid and molten states (green dashed lines, see text). Red lines are guides to the eye. (For interpretation of the references to colour in this figure legend, the reader is referred to the web version of this article.)

calculated functional shape from Eqs. (2) and (3) to obtain the scaling factor (horizontal dotted line in Fig. 2) and the map of effective thickness vs. laser power; replace laser-power scale with temperature scale. The results of the last two steps are illustrated in Fig. 3, where $t_1=14.2$ ns, $t_2=129$ ns, and $t_B=153$ ns (see Eq. (2)). Melting is indicated by a discontinuity in the effective thickness as a function of laser power. The small, yet smooth changes in x-ray intensity over the course of each successful melting run (as observed in the ion chamber data) show that the discontinuity is not due to any abrupt change in physical thickness of the sample. After melting occurs, the effective thickness remains at an approximately constant non-zero value with increasing laser power (Fig. 3). This behavior is explained by tails of the spatial x-ray distribution penetrating cooler regions of the sample. For example, 10% of the total x-ray intensity penetrating sample at about 2000 K would produce a SMS signal equivalent to an effective thickness of four which is comparable to the observed background level.

After the melting experiments were completed, the iron foils were extracted from the DAC and analyzed for signatures of chemical reactions. Using SEM and NanoSIMS instruments at Caltech, we analyzed the recovered melted foils and a pristine foil. We compared concentrations of C, Al, Cl, O, and K impurities, and within the detection limits of each instrument, we found no signature of a chemical reaction in the vicinity of the molten area.

3. Results

3.1. Melting points

The melting point of iron for each experimental run is determined to be the mean of the temperature bounds of the solid and molten states. The error in each melting point is the root-mean-square of the convolution of two probability distributions: (1) the rectangle-shape of the bracketing range from which the mean is determined and (2) the Gaussian-shape of the temperature uncertainty ($\pm$ 100 K). It is known that most materials that are heated in a DAC experience some thermal pressure, with the magnitude varying by sample and its surrounding medium (e.g., Goncharov et al., 2010; Poirier, 2000). For materials with positive thermal expansion, constant volume, the "rigid wall scenario", produces the maximum thermal pressure the material can experience at elevated temperatures (we note this as $P_{th(V)}$). Using our recently determined values of $P_{th(V)}$ for iron obtained from its phonon density of states to 151 GPa (Murphy et al., 2011b), we find that $P_{th(V)}$ at our highest compression point ($P_{300\ K}=70$ GPa) is 23.5 GPa at $T_M=3025$ K. The grey symbols in Fig. 4 show examples from our results with and without consideration of $P_{th(V)}$. At similar PT conditions, recent XRD experiments performed on heated platinum metal in an argon medium showed that the actual thermal pressure was only about half $P_{th(V)}$ (Goncharov et al., 2010). In our experiments, we also expect that some thermal expansion occurred in the heated iron sample (Komabayashi et al., 2009), resulting in a thermal pressure correction smaller than $P_{th(V)}$. We use a similar DAC loading configuration as Goncharov et al. (2010), KCl and iron instead of argon and platinum, and therefore we find it reasonable to assume a similar thermal pressure correction and assign corrections of half $P_{th(V)}$ to our reported melting points (Table 1; red symbols in Figs. 4 and 5).

4. Discussion

4.1. Comparison with other studies

Our data define a different melting trend for compressed iron, compared with several past experimental studies (Figs. 5 and 6).

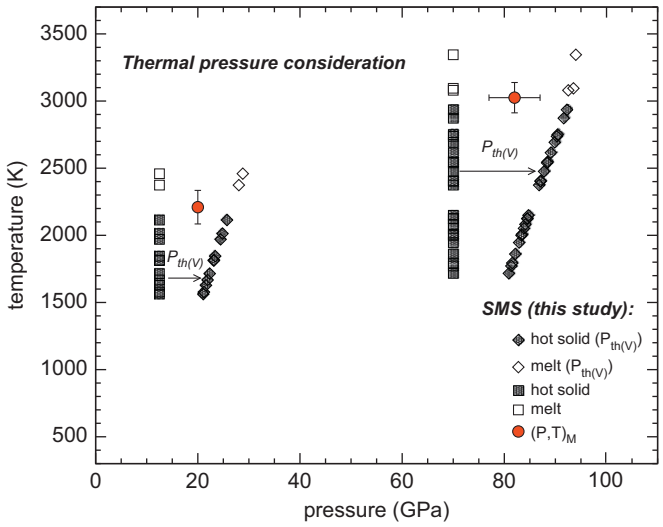

Fig. 4. Thermal pressure consideration for the melting points of iron determined by synchrotron Mössbauer spectroscopy (SMS). Two examples are shown here. Squares have no thermal pressure consideration, diamonds reflect a constant volume thermal pressure, $P_{th(V)}$ (Murphy et al., 2011b), and an arrow indicates $P_{th(V)}$ for the particular data point. Filled red circles: reported melting points considering half $P_{th(V)}$ for the lowest and highest compression points (Table 1). See text for more discussion.

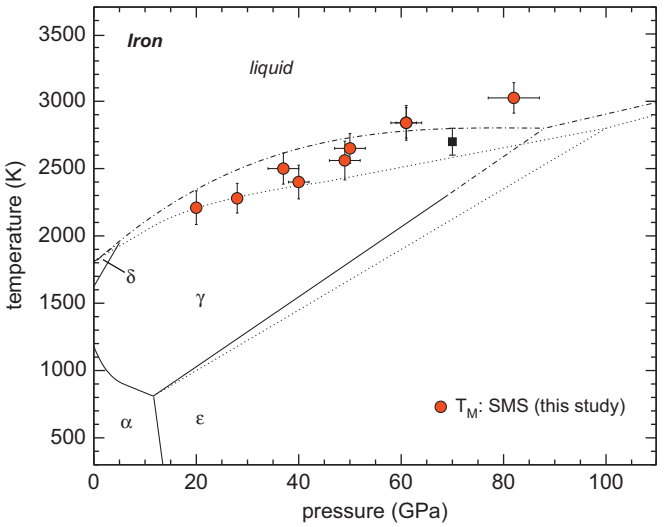

Fig. 5. Melting points of iron as a function of pressure determined from synchrotron Mössbauer spectroscopy (SMS: filled red circles, this study). Our reported melting points consider half $P_{th(V)}$ (Table 1, see text). Literature phase boundaries for iron are also shown. Lines are taken from experimentally reported phase boundaries: $\alpha \leftrightarrow \epsilon$ (Huang et al., 1987), $\gamma \leftrightarrow \delta$ (Strong et al., 1973), $\gamma \leftrightarrow \alpha$ (Bundy, 1965), $\delta \leftrightarrow$ liquid (Sterrett et al., 1965), $\gamma \leftrightarrow \epsilon$ (solid) (Komabayashi et al., 2009), $\gamma \leftrightarrow \epsilon$ (dotted, Boehler, 1986, 1993), $\gamma \leftrightarrow \epsilon \leftrightarrow$ liquid (dash-dotted, Komabayashi and Fei, 2010 using Komabayashi et al., 2009; Shen et al., 1998), $\gamma \leftrightarrow \epsilon \leftrightarrow$ liquid (dotted, Boehler, 1986, 1993; Liu and Bassett, 1975 up to 20 GPa), and $\gamma \leftrightarrow \epsilon \leftrightarrow$ liquid triple point (black filled square, Boehler et al., 2008).

Table 1
Pressure–temperature information for the melting points of iron determined by synchrotron Mössbauer spectroscopy.

$P_{300\ K}$ (GPa)[a]	T_{solid} (K)[b]	T_{melt} (K)[b]	T_M (K)[b]	P (GPa)[c]
12.5 ± 0.5	2080	2340	2210 ± 125	20 ± 0.5
20 ± 3	2200	2360	2280 ± 110	28 ± 3
28 ± 3	2400	2600	2500 ± 115	37 ± 3
32 ± 2	2270	2530	2400 ± 125	40 ± 2
40 ± 3	2380	2740	2560 ± 145	49 ± 3
40 ± 3	2570	2730	2650 ± 110	50 ± 3
50 ± 2	2700	2980	2840 ± 130	61 ± 2
50 ± 3	2750	2930	2840 ± 115	61 ± 3
70 ± 5	2935	3115	3025 ± 115	82 ± 5

[a] Cold pressures ($P_{300\ K}$) are those determined from ruby fluorescence.
[b] Measured temperatures of compressed iron for the last solid, T_{solid}, and first melt, T_{melt}, where the melting point, T_M, is determined to be the mean of these measured values. Uncertainties in the measured temperatures are ± 100 K.
[c] The pressures, P, are those that consider half $P_{th(V)}$ and are plotted as red symbols in Figs. 4 and 5. See text for more details on PT determination and associated uncertainties.

Considering the data around 60 GPa and lower, our melting points fall in between and show some agreement with the shock data for molten *fcc*-iron (Ahrens et al., 2002), studies based on XRD that consider thermal pressure (Komabayashi et al., 2009; Komabayashi and Fei, 2010), and visual observations that did not consider thermal pressure (Boehler, 1986, 1993). The trend in our melting data may be consistent with the melting point reported by Ma et al. (2004) at 105 GPa and $T_M = 3510 \pm 115$ K using XRD, however, thermal pressure was not considered in this XRD study (Fig. 6). For $P \geq 50$ GPa, our melting points occur at higher temperatures than those reported in Boehler (1986, 1993) and Boehler et al. (2008). More specifically, our melting point at our largest compression point is higher than most of these aforementioned melting curves (Boehler, 1986, 1993; Shen et al., 1998; Boehler et al., 2008; Komabayashi et al., 2009) (Fig. 5).

The reason for these differences could originate in the criteria for determining the melting point at high-pressures. In the application of x-ray diffraction techniques to determine melting, it is noted that the x-ray scattering process is non-resonant and extremely fast, i.e., of the order of 10^{-19} s, and atomic motions become irrelevant. An x-ray diffraction pattern represents a series of snapshots of atomic positions, clearly reflecting the spatial order of the sample. In this situation, the disappearance of features such as diffraction lines and the appearance of diffuse scattering upon melting are caused by the loss of long-range order not by a change in atomic mobility. However, such criteria have been difficult to achieve and reproduce at high compressions due to changes in absorption properties and recrystallization of the sample (e.g., Boehler et al., 2008). The SMS method is in contrast to the application of x-ray diffraction techniques to determine melting. The spatial arrangement of the atoms such as crystalline order is not relevant for the collapse of the SMS signal. The disappearance of the SMS signal is strictly based on the dynamical behavior of the atoms, and therefore should help place a tighter constraint on the melting curve of compressed iron.

4.2. Melting of iron at higher-pressures

The Earth's core consists of a solid inner region surrounded by a liquid outer shell, suggesting that the temperature at the ICB corresponds to the melting temperature of core material. The melting point of iron at the ICB provides a tight constraint on the upper bound of the temperature at that point, because studies thus far indicate that all plausible outer core liquids coexist with corresponding inner core alloy solids at or below melting the point of pure iron (e.g., see Alfè et al., 2002a; Asanuma et al., 2010; Terasaki et al., 2011, and references therein). Past estimates of the melting temperature of iron at the ICB have ranged from 4900 (Boehler, 1993) to 7600 ± 500 K (Bass et al., 1987; Williams et al., 1987), which does not permit effective constraints on heat flow and phase relations in the deep Earth (Lay et al., 2008).

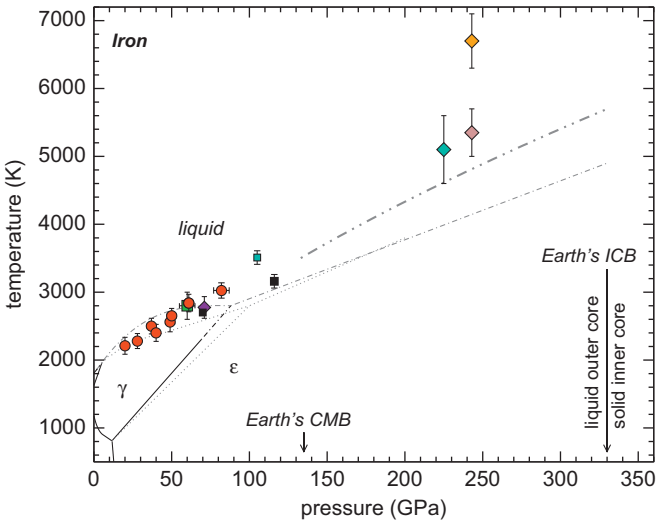

Fig. 6. Phase diagram of iron from experimental studies. The melting points from SMS are shown as red circles (this study). Squares note melting points from *hcp*-iron as reported from XRD: green (Shen et al., 1998), cyan (Ma et al., 2004), and black (Boehler et al., 2008) (P_{th} was not considered in these reports). Diamonds note melting points reported from shock-compression studies: brown (Brown and McQueen, 1986), orange (Bass et al., 1987), violet (Ahrens et al., 2002), and turquoise (Nguyen and Holmes, 2004). The grey dash–dot–dot curve represents the melting curve based on *hcp*-iron's atomic displacements (Murphy et al., 2011b) (see text). Vertical arrows indicate the pressures of Earth's core–mantle (CMB) and inner-core outer-core (ICB) boundaries. Other lines have the same meaning as referenced in Fig. 5. (For interpretation of the references to colour in this figure legend, the reader is referred to the web version of this article.)

At the *PT* conditions of Earth's core, iron is likely to crystallize in the *hcp* structure (Tateno et al., 2010). As we use a method that probes the dynamics of the iron atoms, our results may provide new constraints on the melting curve of *hcp*-iron. Recently, Boehler et al. (2008) suggested the *fcc*-*hcp*-liquid triple point to be at $P=70$ GPa and $T_M=2700\pm100$ K from laser-heated DAC experiments using XRD and the appearance of diffuse scattering to identify melting. Komabayashi et al. (2009) investigated the *fcc*–*hcp* boundary from 21 to 69 GPa using XRD in a DAC with a resistive internal-heating technique and reported the *fcc*–*hcp*–liquid triple point to be at $P=88\pm2$ GPa and $T_M=2800\pm200$ K. The highest compression point obtained in this study (82 ± 5 GPa) falls between the two triple points reported above in terms of pressure. Therefore, it is not clear if the highest compression point that we measured in this study represents melting of *hcp*- or *fcc*-iron. Regardless, the trend in the melting of compressed iron that we observe indicates that iron may have a higher melting point at higher compressions, compared to past studies using diffraction techniques or visual observations.

In an effort to constrain the melting temperature of iron at the pressures of Earth's core, the functional form of its melting curve has been discussed and evaluated recently (Komabayashi and Fei, 2010; Murphy et al., 2011a, 2011b). Murphy et al. (2011b) reported an empirical functional form, $T_M=T_{M0}((P_M-P_{M0})/x+1)^y$, for *hcp*-iron's melting curve based on combining nuclear resonant inelastic x-ray scattering measurements of the mean-square displacement of the iron atoms to 151 GPa, with thermal pressure and anharmonic effects taken into account (see Murphy et al., 2011b for more details). Taking a reference value for *hcp*-iron's melting point from Ma et al. (2004) ($T_{M0}=3510\pm115$ K for iron at 105 GPa, and with full $P_{th(V)}$, $P_{M0}=133.6$ GPa), Murphy et al. (2011b) found $x=158\pm35$ and $y=0.6\pm0.1$, resulting in $T_M=5700\pm150$ K at the ICB pressure of 330 GPa (depth of 5150 km) (see Murphy et al., 2011b, for more details) (Fig. 6). The uncertainty reported here is the root-mean-square of the assumed error in the reference melting temperature (±115 K) and melting curve shape (±100 K, Murphy et al., 2011b). The predicted melting temperature of iron at the ICB from this procedure is based on using an anchor point that used different criteria for melting than the current study, while assuming full thermal pressure was experienced by the hot iron sample. Nevertheless, this particular melting curve is in good agreement with the shock data of Nguyen and Holmes (2004), but lower than the range reported by Brown and McQueen (1986) and Bass et al. (1987) (Fig. 6). The *ab initio* melting curve based on combining the free energy of *hcp*-iron (Alfè et al., 2001) with theoretical liquid-state free energy predicts $T_M=6350\pm600$ K (Alfè et al., 2002b). These values are loosely consistent with static compression XRD experiments that report the presence of solid *hcp*-iron at 377 ± 10 GPa and 5700 ± 250 K (Tateno et al., 2010).

5. Conclusions

We present a new method of detecting the solid–liquid phase boundary of compressed iron by monitoring the dynamics of the iron atoms using synchrotron Mössbauer spectroscopy. Our reported melting points for iron at low-pressures are in very good agreement with past reports. However, our melting points define a trend with pressure that is different from past studies. In this study, we find $T_M=3025\pm115$ K for iron at 82 ± 5 GPa (near the *fcc*–*hcp*–liquid triple point), which is significantly higher than what has been reported based on XRD that considered thermal pressure (Komabayashi and Fei, 2010), XRD without thermal pressure consideration (Boehler et al., 2008), and visual observations (Boehler, 1993). Differences could be explained by the different melting criteria used, as discussed above. At higher pressures than those sampled in this study, the trend in our melting data may suggest higher melting temperatures for *hcp*-iron, as reported in shock measurements (e.g., Nguyen and Holmes, 2004), *ab initio* simulations (e.g., Alfè et al., 2002b), and melting behavior based on the mean-square displacement of the iron atoms (Murphy et al., 2011b).

The results of this study represent a significant step toward a reliable melting curve of iron at Earth's core conditions. Although the Earth's core is mainly composed of iron, the seismologically inferred density requires the presence of light elements to balance the density deficit. Experimental and theoretical investigations suggest that light elements such as S, O, and Si alloyed with iron could depress the melting point of pure iron by up to ~700 K at the ICB (e.g., Alfè et al., 2002a; Terasaki et al., 2011). Certainly, more experiments are required to fully constrain the melting curve of *hcp*-iron and candidate alloys at core pressures and temperatures. For other terrestrial planets possessing cores with liquid portions rich in metallic iron, such as Mercury and Mars, the higher melting temperatures we obtain for compressed iron may imply warmer internal temperatures of these planets. With iron being a dominant component of candidate alloys in terrestrial cores and a main constituent in the mineralogy of most mantles in terrestrial planets, this method should provide a unique complement to existing methods for determining and constraining the melting curves of such phases under high-pressure conditions.

Acknowledgements

We thank D.L. Lakstanov for help with experiments, G. Shen, D. Zhang, H.-K. Mao, and P.D. Asimow for helpful discussions, and the NSF and Caltech for support of this research. We thank two anonymous reviewers and the editor, L. Stixrude, for helpful comments and suggestions. Use of the Advanced Photon Source

was supported by the U.S. D.O.E., O.S., O.B.E.S. (DE-AC02-06CH11357). Sector 3 operations are partially supported by COMPRES (NSF EAR 06-49658). SEM and nanoSIMS analyses were carried out at the Caltech GPS Division Analytical Facility (funded in part by the MRSEC Program of the NSF under DMR-0080065).

References

Ahrens, T.J., Holland, K.G., Chen, G.Q., 2002. Phase diagram of iron, revised-core temperatures. Geophys. Res. Lett. 29, http://dx.doi.org/10.1029/2001GL014350.

Alfè, D., 2009. Temperature of the inner-core boundary of the earth: melting of iron at high pressure from first-principles coexistence simulations. Phys. Rev. B 79.

Alfè, D., Gillan, M., Price, G., 1999. The melting curve of iron at the pressures of the Earth's core from ab initio calculations. Nature 401, 462–464.

Alfè, D., Gillan, M.J., Price, G.D., 2002a. Composition and temperature of the Earth's core constrained by combining ab initio calculations and seismic data. Earth Planet. Sci. Lett. 195, 91–98.

Alfè, D., Price, G.D., Gillan, M.J., 2001. Thermodynamics of hexagonal-close-packed iron under earth's core conditions. Phys. Rev. B 64, 045123.

Alfè, D., Price, G.D., Gillan, M.J., 2002b. Iron under Earth's core conditions: liquid-state thermodynamics and high-pressure melting curve from ab initio calculations. Phys. Rev. B 65, 165118.

Anderson, O.L., 1990. The high pressure triple points and their effect on the heat flow from the Earth's core. J. Geophys. Res. 95, 21697–21707.

Andrault, D., Bolfan-Casanova, N., Ohtaka, O., Fukuis, H., Arima, H., Fialin, M., Funakoshi, K., 2009. Melting diagrams of Fe-rich alloys determined from synchrotron in situ measurements in the 15–23 GPa pressure range. Phys. Earth Planet. Inter. 174, 181–191.

Asanuma, H., Ohtani, E., Sakai, T., Terasaki, H., Kamada, S., Kondo, T., Kikegawa, T., 2010. Melting of iron–silicon alloy up to the core–mantle boundary pressure: implications to the thermal structure of the Earth's core. Phys. Chem. Miner. 37, 353–359.

Bass, J.D., Svendsen, B., Ahrens, T.J., 1987. The temperature of shock compressed iron. In: Manghnani, M.H., Syono, Y. (Eds.), High-Pressure Research in Mineral Physics, pp. 393–402.

Bergmann, U., Shastri, S.D., Siddons, D.P., Batterman, B.W., Hastings, J.B., 1994. Temperature dependence of nuclear forward scattering of synchrotron radiation in alpha ^{57}Fe. Phys. Rev. B 50 (9), 5957–5961.

Boehler, R., 1986. The phase diagram of iron at 430 kbar. Geophys. Res. Lett. 13, 1153–1156.

Boehler, R., 1992. Melting of the Fe–FeO and Fe–FeS systems at thigh pressure: constraints on core temperatures. Earth Planet. Sci. Lett. 111, 217–227.

Boehler, R., 1993. Temperatures in the Earth's core from melting-point measurements of iron at high static pressures. Nature 363, 534–536.

Boehler, R., Santamaría-Pérez, D., Errandonea, D., Mezouar, M., 2008. Melting, density, and anisotropy of iron at core conditions: new x-ray measurements to 150 GPa. J. Physics: Conf. Ser. 121, http://dx.doi.org/10.1088/1742-6596/121/2/022018.

Boyle, A.J.F., Bunbury, S.S.P., Edwards, C., Hall, H.E., 1961. The Mössbauer effect in tin from 120 K to the melting points. Proc. Phys. Soc. 77, 129–135.

Brown, J.M., McQueen, R.G., 1986. Phase transitions, Grüneisen parameter, and elasticity for shocked iron between 77 GPa and 400 GPa. J. Geophys. Res. 91, 7485–7495.

Bundy, F.P., 1965. Pressure–temperature phase diagram of iron to 200 kbar, 900 °C. J. Appl. Phys. 36, 616–620.

Chen, B., Li, J., Hauck, S.A., 2008. Non-ideal liquidus curve in the Fe–S system and Mercury's snowing core. Geophys. Res. Lett. 35, http://dx.doi.org/10.1029/2008GL033311.

Fei, Y., Bertka, C.M., 2005. The interior of Mars. Science 308, 1120–1121.

Fei, Y., Bertka, C.M., Finger, L.W., 1997. High-pressure iron–sulfur compound Fe_3S_2, and melting relations in the system Fe–FeS. Science 275, 1621–1623.

Fei, Y., Prewitt, C.T., Mao, H.K., Bertka, C.M., 1995. Structure and density of FeS at high pressure and high temperature and the internal structure of Mars. Science 268, 1892–1894.

Giefers, H., Lübbers, R., Rupprecht, K., Wortmann, G., Alfè, D., Chumakov, A.I., 2002. Phonon spectroscopy of oriented hcp iron. High Press. Res. 22, 501–506.

Goncharov, A.F., Prakapenka, V.B., Struzhkin, V.V., Kantor, I., Rivers, M.L., Dalton, D.A., 2010. X-ray diffraction in the pulsed laser heated diamond anvil cell. Rev. Sci. Instrum. 81, 5–11.

Heinz, D.L., Jeanloz, R., 1987. Temperature measurements in the laser-heated diamond anvil cell. In: High-Pressure Research in Mineral Physics. Terra Sci. Tokyo, pp. 113–127.

Hemley, R.J., Mao, H.K., 2001. In situ studies of iron under pressure: new windows on the Earth's core. Int. Geol. Rev. 43, 1–30.

Huang, E., Bassett, W.A., Weathers, M.S., 1987. Phase relationships in Fe–Ni alloys at high pressures and temperatures. J. Geophys. Res. 93, 7741–7746.

Kagan, Y., Afanas'ev, A.M., Kohn, V.G., 1979. On excitation of isomeric nuclear states in a crystal by synchrotron radiation. J. Phys. C: Solid State Phys. 12, 615–631.

Komabayashi, T., Fei, Y., 2010. Internally consistent thermodynamic database for iron to the Earth's core conditions. J. Geophys. Res. 115 (B3).

Komabayashi, T., Fei, Y., Meng, Y., Prakapenka, V., 2009. In-situ x-ray diffraction measurements of the gamma—epsilon transition boundary of iron in an internally-heated diamond anvil cell. Earth Planet. Sci. Lett. 282 (1–4), 252–257.

Laio, A., Bernard, S., Chiarotti, G.L., Scandolo, S., Tosatti, E., 2000. Physics of iron at Earth's core conditions. Science 287, 1027–1030.

Lay, T., Hernlund, J., Buffett, B.A., 2008. Core–mantle boundary heat flow. Nat. Geosci. 1 (January (1)), 25–32, URL http://dx.doi.org/10.1038/ngeo.2007.44.

Lehmann, I., 1936. P'. Publ. Bur. Cent. Seismol. Int. 14, 87–115.

Lin, J.F., Sturhahn, W., Zhao, J., Shen, G., Mao, H.K., Hemley, R.J., 2004. Absolute temperature measurement in a laser-heated diamond anvil cell. Geophys. Res. Lett. 31, L14611.

Liu, L.G., Bassett, W.A., 1975. The melting of iron up to 200 kbar. J. Geophys. Res. 81, 3777–3782.

Ma, Y., Somayazulu, M.S., Shen, G., Mao, H.K., Shu, J., Hemley, R.J., 2004. In situ X-ray diffraction studies of iron to Earth-core conditions. Phys. Earth Planet. Inter. 143–144, 455–467.

Mao, H.K., Bell, P.M., Hadidiacos, C., 1987. Experimental phase relations of iron to 360 kbar and 1400 C, determined in an internally heated diamond anvil apparatus. In: Manghnani, M., Syono, Y. (Eds.), High Pressure Research in Mineral Physics. Terra Scientific/AGU, pp. 135–138.

Mao, H.K., Xu, J., Bell, P.M., 1986. Calibration of the ruby pressure gauge to 800 kbar under quasi-hydrostatic conditions. J. Geophys. Res. 91, 4673–4676.

Mao, H.K., Xu, J., Struzhkin, V.V., Shu, J., Hemley, R.J., Sturhahn, W., Hu, M.Y., Alp, E.E., Vocadlo, L., Alfè, D., Price, G.D., Gillan, M.J., Schwoerer-Böhning, M., Häusermann, D., Eng, P., Shen, G., Giefers, H., Lübbers, R., Wortmann, G., 2001. Phonon density of states of iron up to 153 Gigapascals. Science 292, 914–916.

Margot, J.L., Peale, S.J., Jurgens, R.F., Slade, M.A., Holin, I.V., 2007. Large longitude libration of Mercury reveals a molten core. Science 316, 710–714.

McDonough, W.F., 2003. Compositional model for the Earth's core. In: Carlson, R.W. (Ed.), Treatise on Geochemistry, vol. 2. Elsevier, New York, pp. 547–568.

McDonough, W.F., Sun, S.S., 1995. The composition of the Earth. Chem. Geol. 120, 223–253.

Mössbauer, R.L., 1958. Kernresonanzfluoreszenz von gammastrahlung in ^{191}Ir. Z. Phys. 151, 124–143.

Murphy, C.A., Jackson, J.M., Sturhahn, W., Chen, B., 2011a. The Grüneisen parameter of hcp-iron to 171 GPa. Geophys. Res. Lett. L24306, http://dx.doi.org/10.1029/2011GL049531.

Murphy, C.A., Jackson, J.M., Sturhahn, W., Chen, B., 2011b. Melting and thermal pressure of hcp-Fe from the phonon density of states. Phys. Earth Planet. Inter. 188, http://dx.doi.org/10.1016/j.pepi.2011.07.001.

Nguyen, J.H., Holmes, N.C., 2004. Melting of iron at the physical conditions of the Earth's core. Nature 427, 339–341.

Poirier, J.-P., 2000. Introduction to the Physics of the Earth's Interior, 2nd ed. Cambridge University Press.

Shen, G., Mao, H.K., Hemley, R.J., Duffy, T.S., Rivers, M.L., 1998. Melting and crystal structure of iron at high pressures and temperatures. Geophys. Res. Lett. 25, 373–376.

Shen, G., Rivers, M., Wang, Y., Sutton, S., 2001. Laser heated diamond cell system at the advanced photon source for in situ x-ray measurements at high pressure and temperature. Rev. Sci. Instrum. 72, 1273.

Shen, G., Sturhahn, W., Alp, E.E., Zhao, J., Toellner, T.S., Prakapenka, V.B., Meng, Y., Mao, H.-K., 2004. Phonon density of states in iron at high pressures and high temperatures. Phys. Chem. Miner. 31, 353–359.

Singwi, K.S., Sjölander, A., 1960. Resonance absorption of nuclear gamma rays and the dynamics of atomic motions. Phys. Rev. 120, 1093–1102.

Smith, D.E., Zuber, M.T., Phillips, R.J., Solomon, S.C., II, S.A.H., Lemoine, F.G., Mazarico, E., Neumann, G.A., Peale, S.J., Margot, J.L., Johnson, C.L., Torrence, M.H., Perry, M.E., Rowlands, D.D., Goossens, S., Head, J.W., Taylor, A.H., 2012. Gravity field and internal structure of Mercury from MESSENGER. Science 336, 214–217.

Sola, E., Alfè, D., 2009. Melting of iron under Earth's core conditions from diffusion Monte Carlo energy calculations. Phys. Rev. Lett. 103, 078501.

Sterrett, K.F.J., Klement, W.J., Kennedy, G.C., 1965. Effect of pressure on the melting of iron. J. Geophys. Res. 70, 1979–1984.

Stevenson, D.J., 2001. Mars' core and magnetism. Nature 412, 214–219.

Stewart, A.J., Schmidt, M.W., van Westrenen, W., Liebske, C., 2007. Mars: a new core-crystallization regime. Science 316, 1323–1325.

Stixrude, L., Wasserman, E., Cohen, R.E., 1997. Composition and temperature of Earth's inner core. J. Geophys. Res. 102, 24729–24739.

Strong, H.M., Tuft, R.E., Hanneman, R.E., 1973. The iron fusion curve and alpha-gamma-liquid triple point. Metall. Trans. 4, 2657–2661.

Sturhahn, W., 2000. CONUSS and PHOENIX: evaluation of nuclear resonant scattering data. Hyperfine Interact. 125, 149–172.

Sturhahn, W., 2004. Nuclear resonant spectroscopy. J. Phys.: Condens. Matter 16, S497–S530.

Sturhahn, W., Chumakov, A.I., 1999. Lamb–Mössbauer factor and second-order Doppler shift from inelastic nuclear resonant absorption. Hyperfine Interact. 123–124, 809–824.

Sturhahn, W., Jackson, J.M., 2007. Geophysical applications of nuclear resonant scattering. In: Geological Society of America Monograph. Geological Society of America.

Tateno, S., Hirose, K., Ohishi, Y., Tatsumi, Y., 2010. The structure of iron in Earth's inner core. Science 330, 359–361.

Terasaki, H., Kamada, S., Sakai, T., Ohtani, E., Hirao, N., Ohishi, Y., 2011. Liquidus and solidus temperatures of a Fe–O–S alloy up to the pressures of the outer core: implication for the thermal structure of the Earth's core. Earth Planet. Sci. Lett. 304, 559–564.

Toellner, T.S., 2000. Monochromatization of synchrotron radiation for nuclear resonant scattering experiments. Hyperfine Interact. 125, 3–28.
Toellner, T.S., Hu, M.Y., Sturhahn, W., Quast, K.W., Alp, E.E., 1997. Inelastic nuclear resonant scattering with sub-meV energy-resolution. Appl. Phys. Lett. 71, 2112–2114.
Williams, Q., Jeanloz, R., Bass, J., Svendsen, B., Ahrens, T., 1987. The melting curve of iron to 250 GPa: a constraint on the temperature at Earth's center. Science 236, 181–182.
Yoo, C.S., Holmes, N.C., Ross, M., 1993. Shock temperatures and melting of iron at Earth core conditions. Phys. Rev. Lett. 70, 3931–3934.
Zhao, J., Shen, G., Sturhahn, W., Alp, E.E., 2004a. Highly efficient gaseous loading technique for diamond anvil cells. Rev. Sci. Instrum. 75, 5149–5151.
Zhao, J., Sturhahn, W., Lin, J.-F., Shen, G., Alp, E.E., Mao, H.-K., 2004b. Nuclear resonant scattering at high pressure and high temperature. High Pressure Res. 24, 447–457.